PERGAMON

International Journal of Heat and Mass Transfer 44 (2001) 2889–2902

International Journal of HEAT and MASS TRANSFER

www.elsevier.com/locate/ijhmt

Visualization of roll patterns in Rayleigh–Bénard convection of air in a rectangular shallow cavity

J.T. Lir, T.F. Lin *

Department of Mechanical Engineering, National Chiao Tung University, 1000 Ta Hsueh Road, Hsinchu 30010, Taiwan, ROC

Received 5 May 2000; received in revised form 9 October 2000

Abstract

Flow visualization is conducted here to study the vortex flow patterns associated with the Rayleigh–Bénard convection in a horizontal shallow cavity of air. The cavity is a rectangular enclosure characterized by the aspect ratios $A_x = 16$ and $A_z = 20$. Attention is focused on the convection rolls driven at slightly supercritical and subcritical buoyancies. The results show that at slightly subcritical *Ra* the induced vortex flow is in the form of rectangular rolls along the cavity sides and short straight parallel rolls in the cavity core. At slightly higher *Ra* near Ra_{c_∞} $(= 1708)$ more rectangular rolls appear and the short straight rolls in the cavity core merge together to form a serpentine roll. At slightly supercritical buoyancy with $2000 \leqslant Ra \leqslant 3000$ the entire cavity is filled with the straight rolls all parallel to the short sides of the cavity. At an even higher *Ra* of 4000 the vortex rolls become irregular and time dependent. Moreover, the processes through which various vortex flow structures evolve during the transient stage are shown to be rather complicate and the vortex flow patterns during the flow formation are significantly affected by the heating rate in raising the buoyancy force. Furthermore, the wavenumber reduction at higher *Ra* for the parallel vortex roll pattern was noted to mainly result from the splitting of some rectangular rolls into cells and the subsequent merging of the cells into bigger rolls at the intermediate stage of the flow formation.

1. Introduction

Buoyancy-driven cellular flow structure in a bottom heated horizontal shallow enclosure, noted as the Rayleigh–Bénard convection, has been extensively investigated over the past four decades due to the important role it plays in fundamental fluid mechanics and heat transfer study and in technological applications such as solar energy collection, cooling of microelectronic equipments, heat transfer in nuclear reactors, growth of single crystal from fluid phase and many others. The resulting vortex flow patterns are relatively complicated and are very sensitive to the physical and geometrical parameters and thermal boundary conditions. Convection rolls in the form of transverse rolls parallel with the short or long side of rectangular cavity, cross rolls, circular rolls, knotted rolls, incomplete rolls, square cells, etc. were reported in the literature. Comprehensive review of the roll patterns and the associated heat transfer has been given by Ostrach [1], Yang [2] and Koschmieder [3]. In what follows, the relevant literature on the thermal convection in a bottom heated horizontal rectangular shallow cavity, which is the subject of the present study, is briefly reviewed.

Davis [4] and Catton [5] used the linear stability theory to predict the critical Rayleigh number Ra_c for the onset of convection in a horizontal layer. The critical Rayleigh number measured by Behringer and Ahlers [6] for helium and by Koschmieder and Pallas [7] for silicone oil was found to be only a function of the boundary conditions.

For buoyancy slightly beyond the convective threshold with $Ra > Ra_{c^\infty}$ $(= 1708)$ square cells are induced in square and circular layers of silicone oil and syrup, as noted by Koschmieder [3], LeGal et al. [8] and White [9]. The square cells are formed from the superimposition of rolls parallel to the walls of the square frame. Edward [10] found crossed rolls at the onset of

* Corresponding author. Tel.: +886-35-712121; fax: +886-35-720634.

E-mail address: u8614812@cc.nctu.edu.tw (T.F. Lin).

0017-9310/01/$ - see front matter
PII: S0017-9310(00)00340-9

Nomenclature

A_x, A_z	aspect ratios, b/d and l/d
b, l, d	channel width, length and height
G	gravitational acceleration
Ra	Rayleigh number $\beta g d^3 (T_h - T_c)/\alpha v$
Ra_{c_∞}	critical Rayleigh number corresponding to the onset of convection for an infinite layer
T	time, s
T_c, T_h	temperatures of the cold and hot plates
x, y, z	dimensionless Cartesian coordinates scaled with d
α	thermal diffusivity
β	thermal expansion coefficient
v	kinematic viscosity

convection in boxes with the aspect ratios A_x and A_z below 5. In a rectangular layer the convection rolls were found to be parallel to the shorter sides of the layer for a slightly supercritical Rayleigh number by a number of investigators [4,11–18] based on some theoretical analyses and experimental measurement. At higher supercritical Rayleigh numbers the induced flow in high Prandtl number fluids tends to become distinctly three-dimensional. Additional new rolls are generated at right angles to the base rows, which eventually lead to bimodal convection [19]. At increasing buoyancy the convection rolls deform through the zigzag, skew-varicose, knot, oscillatory and cross-roll instabilities [20–25]. The strong dependence of the instabilities on the Prandtl number of the fluid was noted. At an even higher buoyancy three-dimensional time-dependent oscillatory convection was revealed by Clever and Busse [26–28]. The associated flow is rather complex.

Another issue is the variation of the preferred wave number of the convection rolls with the Rayleigh number in the near supercritical region. Experimental data have consistently shown that the wave number decreases as the Rayleigh number increases [7,29]. This is noted as the skewed varicose instability. Busse and Clever [30] indicated that the reduction in the wave number at increasing Ra, sometimes due to the loss of convection rolls, was either caused by three-dimensional instabilities or by the presence of the vertical side walls. More detailed observation of the skewed varicose instability was later conducted by Leith and his colleagues [31–33] for an air layer.

In subcritical buoyancy Koschmieder [3] pointed that some weak cellular flow can be induced by imperfect bifurcations with the motions beginning with infinitesimal amplitude. In the experiments with bounded fluid layer she further showed that the onset of convection usually proceeded from subcritical motion at the walls. Pictures of subcritical rolls along a circular wall can be found in [7].

The above literature review clearly indicates that there have been a lot of results reported in the past for thermal convection in a bottom heated shallow cavity covering various aspects of the driven flow. But the vortex flow patterns induced in the thermal cavity convection at a low Rayleigh number near the critical level remain largely unexplored. In the present study flow visualization is conducted to unravel the cellular flow structures driven by the Rayleigh–Bénard convection in a shallow horizontal cavity of air mainly for slightly supercritical and subcritical buoyancies for Ra ranging from 1500 to 4000. In addition to the induced steady flow, the time-dependent flow patterns and the evolution of the flow leading to various vortex flow patterns will be inspected in detail.

2. Experimental apparatus and procedures

A schematic of the test section used here to examine the cellular flow structure in the Rayleigh–Bénard convection in a horizontal shallow enclosure of air is depicted in Fig. 1(a). The shallow cavity is characterized by

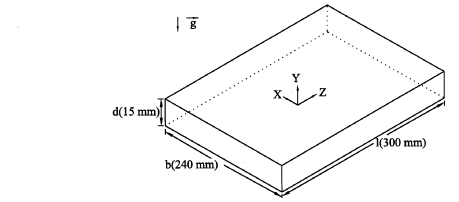

(a)

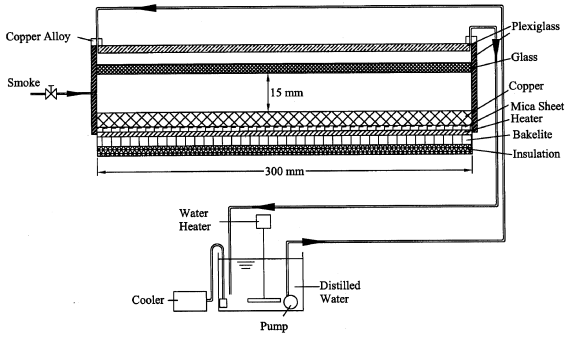

(b)

Fig. 1. Schematic of test section (a) and cross-section view of the cavity showing the design of the horizontal plates (b).

a small height of 15 mm along with much larger width of 240 mm and length of 300 mm, providing the cavity aspect ratios of $A_x = 16$ and $A_z = 20$. To procure the required uniform thermal boundary condition, the bottom of the cavity is made of a 20 mm thick, high-purity copper plate and is heated by D.C. power supplies. In order to insure the bottom plate to be uniformly heated, the heaters attached onto the outside surface of the bottom copper plate are divided into 10 segments and each heater is independently controlled by a GW GPC 3030D laboratory power supply. The top of the test section is made of a three layer structure – a 3 mm thick glass plate and a 2 mm thick plexiglass plate above it with a gap width of 3 mm between them. This top glass plate is reinforced by copper alloy frames to keep it flat. Distilled water is provided from a tank and flows into this gap to cool the glass plate. The distilled water is maintained at a constant temperature by a constant temperature circulation unit that consists of a cooler, a heater and a 200 l distilled water reservoir. This cooling unit can control the temperature of the distilled water within ± 0.1°C. The water flow rate is adjusted carefully to keep the temperature difference over the glass plate within ± 0.1°C. The water head is also suitably adjusted to minimize any possible deformation in the glass plate. The details of the horizontal hot and cold plates are illustrated in Fig. 1(b). The side walls of the enclosure are made of 5 mm thick plexiglass plates. The whole enclosure is thermally insulated with a superlon insulator of 20 mm thick and is bounded on a rigid supporting frame.

The temperature of the test section is monitored by 13 calibrated and electrically insulated copper–constantan (T-type) thermocouples embedded in the bottom copper plate and 6 T-type thermocouples stuck to the inside surface of the top glass plate. The temperature of both plates could be maintained at nearly uniform and constant values with the deviations ranging from ± 0.05 to ± 0.12°C. The thermocouple signals are recorded by the Computer Products RTP 743 data acquisition system with a resolution of ± 0.05°C.

Flow visualization is performed by injecting incense smoke into the cavity before each experiment. By using a 1.5–2.5 mm plane light beam of an overhead projector with an adjustable knife-edge to illuminate the flow field containing these smoke particles, a sharp contrast could be obtained between the cavity walls and the smoke. For each case in the experiment we first turn on the D.C. power supplies to raise the bottom plate temperature. Meanwhile, the distilled water is circulated over the top plate. Each case takes about three hours to raise the Rayleigh number to the test point and another two hours are needed to maintain the cellular vortex flow at the stable or statistically stable state. After this we start flow visualization. For the transient tests to observe the vortex flow formation the Rayleigh number is changed to the test point in about 5–10 min to account for the thermal inertia of the horizontal plates.

In order to reduce any possible bias and data reduction errors between the true physical value and the readout of the sensors and transducers, the data acquisition systems and various instruments including multiplexers (Computer Products RTP 743), a digital barometer (Drunk Products DPI-260) and reference junctions (Celesco Transducer Products BRJ14) are calibrated and adjusted end-to-end on site by the Instrument Calibration Section, Q.A. Center, Chung Shan Institute of Science and Technology (CSICI), Taiwan, with the transfer standards that the calibration hierarchy can trace back to the standard of National Institute of Standard and Technology (NIST), USA. Before performing the end-to-end calibration all the sensors and transducers used were transported to CSIST for calibration or adjustment with the inter-lab standards based on the test points that will be encountered in the present test to get the best calibration curve-fit data. The data reduction error is reduced further by using the best nonlinear least square calibration curve-fits and by selecting a suitable gain code of the multiplexers.

Uncertainties in the Rayleigh number and other independent parameters are calculated according to the standard procedures established by Kline and McClintock [34]. The uncertainties of the thermophysical properties of air are included in the analysis. The fluid properties are real-time corrected based on the temperature detected at the test section. In addition, the uncertainties of the control unsteadiness and temperature non-uniformity are accounted for in the evaluation of the data uncertainty. The analysis shows that the uncertainties of temperature, dimensions and Rayleigh number measurements are estimated to be less than ± 0.05°C, ± 0.05 mm and $\pm 5\%$, respectively.

3. Results and discussion

Selected flow photos from the present study are presented in the following to illustrate the Rayleigh–Bénard convection roll patterns in the shallow cavity investigated here at slightly supercritical and subcritical buoyancies. Attention will be particularly paid to the flow patterns at steady state or statistical state when the flow does not reach steady state for a sufficiently long period of time. Meanwhile, the evolution processes through which various flow patterns are formed will be examined in detail.

3.1. Convection rolls at steady and statistical states

The buoyancy-driven vortex flow structures in the cavity at long time when the initial transients all disap-

pear are inspected first. Fig. 2 shows the top view photos taken at the midheight of the cavity $y = 1/2$ for various Rayleigh numbers including the subcritical and supercritical buoyancies. These results indicate that at a slightly supercritical buoyancy for $2000 \leqslant Ra \leqslant 3000$ the flow is dominated by the straight vortex rolls of nearly equal diameter with their axes all parallel to the short sides of the cavity, as evident from Figs. 2(e)–(g). This parallel roll structure along the short sides is in agreement with the results from some previous investigations

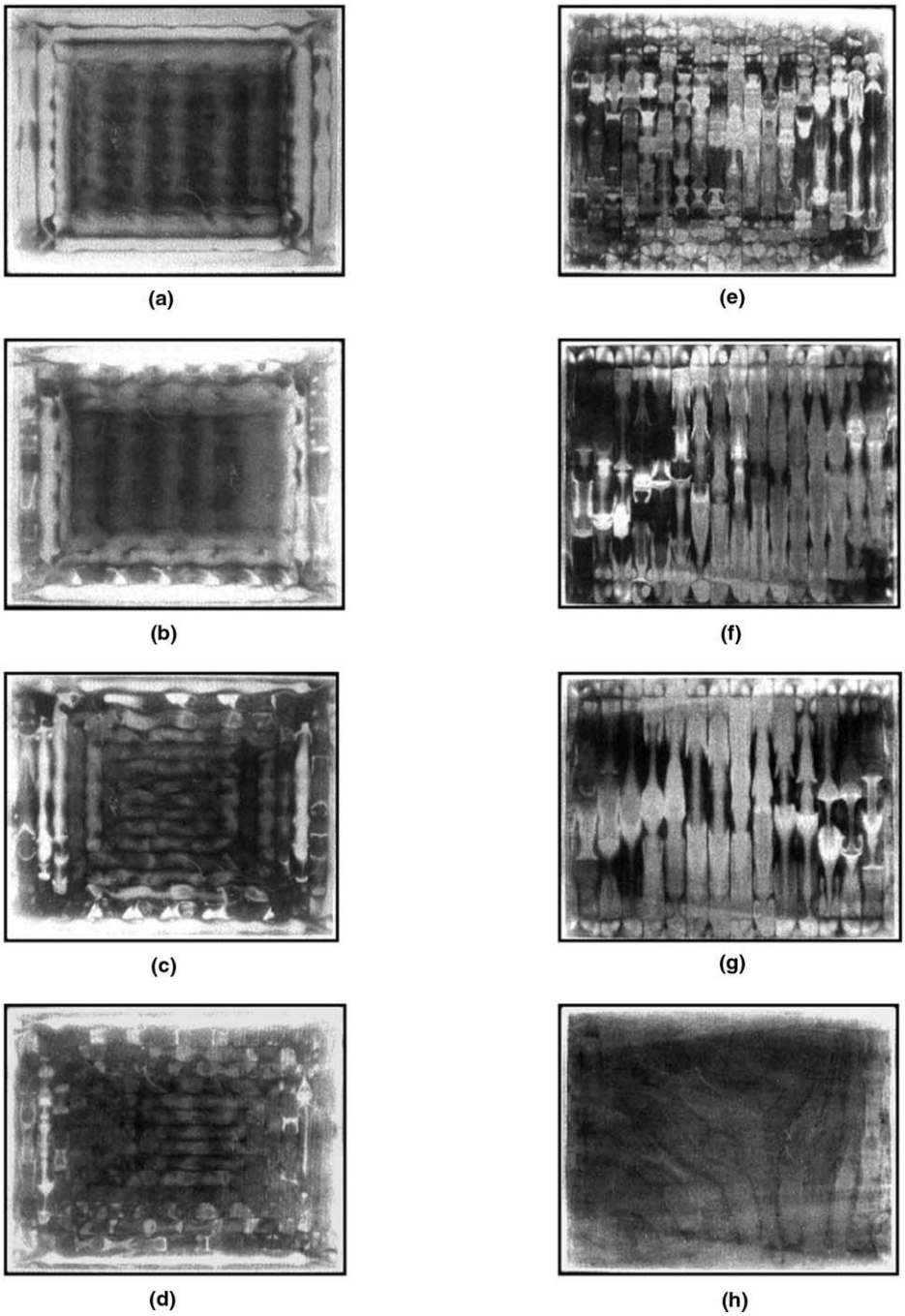

Fig. 2. Top view flow photos at steady or statistical state for: (a) $Ra = 1500$, (b) $Ra = 1600$, (c) $Ra = 1750$, (d) $Ra = 1850$, (e) $Ra = 2000$, (f) $Ra = 2500$, (g) $Ra = 3000$ and (h) $Ra = 4000$.

[11–18,35]. We also note that the rolls are larger for a higher *Ra*. More specifically, there are 20, 18 and 16 rolls in the cavity, respectively, for $Ra = 2000$, 2500, 3000. Thus the roll diameter increases from d to $1.25d$ for Ra raised from 2000 to 3000. This wavenumber reduction with the increase in the Rayleigh number, noted as the skewed varicose instability, agrees qualitatively with that in the literature [23,31–33]. The instability mechanism in this wavenumber reduction processes will be examined later when we discuss the formation of the roll structures. When *Ra* is raised further to 4000, the vortex rolls become curved and are somewhat irregular. The driven flow is in fact time-dependent and Fig. 2(h) shows the planform of the structure at some arbitrary time instant in the statistical state.

It is of interest to note that at slightly subcritical buoyancy for $Ra = 1500$ and 1600 the resulting steady vortex flow is in the form of a few rectangular rolls along the cavity sides (Figs. 2(a) and (b)) and several nearly straight rolls parallel to the short sides of the cavity in the cavity core. In fact, we have four rectangular rolls and ten short parallel rolls which are relatively weak in each cavity. A close inspection of the straight rolls, however, reveals that the outer boundaries of these rolls are slightly sinuous. For a small raise of *Ra* to 1750 and 1850, more rectangular rolls are induced and the sinuous short rolls split into cells. The cells then gradually merge into a serpentine roll (Figs. 2(c) and (d)).

To further reveal the structure of the induced convection rolls, the flow photos viewing from the short and long sides of the cavity are presented in Figs. 3 and 4 along with the planforms of the corresponding vortex flows. The results in Fig. 3 clearly indicate that away from the cavity sides the flow is dominated by the regular parallel rolls of equal diameter. But the two rolls near the short sides of the cavity are much larger than these regular rolls. Moreover, near the long sides of the cavity the vortex rolls are somewhat irregular. Merging of the adjacent rolls can be seen in this side wall region. Next, the vortex flow pattern viewing, respectively, from the long and short sides of the cavity for the subcritical case with $Ra = 1500$ given in Fig. 4 indicates that the rectangular roll directly contacting the cavity sides is also much larger than the other rectangular rolls. Note that near the corners of the cavity where the short legs and long legs of the rectangular rolls merge together the vortex flow is somewhat irregular. Besides, at this low buoyancy the rectangular rolls are not fully established especially for those away from the cavity sides and parallel to the short sides. Specifically, the deformation of the outside boundaries of these rolls is clearly observed (Fig. 4(a)). Moreover, the flow photos taken from the long sides (Fig. 4(c)) further confirm that the short parallel rolls in the cavity core are relatively weak and the roll boundaries are somewhat obscure.

3.2. Formation of convection rolls

In the study of the vortex roll formation the experiment is started by raising the Rayleigh number to the value required for a specific case to be investigated. In view of the thermal inertia of the bottom and top plates, it takes a certain period of time to raise the Rayleigh number to the target level. The formation of the vortex flow containing the rectangular rolls and parallel short rolls at slightly subcritical buoyancy is illustrated in Fig. 5 by showing the top view flow photos for the case with $Ra = 1600$ at various instants of time following the raise of the Rayleigh number. The time $t = 0$ denotes the instant at which we begin to raise the Rayleigh number. Initially for $t < 0$, the flow in the cavity is quiescent since $Ra = 0$. Note that it takes 300 s to raise *Ra* to 1600. The results in Fig. 5 show that shortly after the transient is started no noticeable flow motion is induced in the cavity (Fig. 5(a)). Slightly later, relatively weak straight rolls appear along the sides of the cavity (Figs. 5(b) and (c)). The structure of the rectangular rolls is clearly seen. As time proceeds, the existing rolls strengthen and more rectangular rolls are induced (Figs. 5(d)–(h)). Meanwhile, relatively weak straight rolls parallel to the short sides of the cavity start to show up in the cavity core surrounded by the rectangular rolls. As the processes continue, the parallel rolls in the cavity core gradually grow in intensity, so do the newly formed rectangular rolls (Figs. 5(i)–(k)). Finally, a vortex flow pattern comprising of rectangular rolls near the cavity sides and parallel short rolls in the cavity core is formed (Fig. 5(l)). It is of interest to mention that the above flow formation processes are rather slow and it takes more than 75 min for the vortex flow to evolve to its final state.

Next, the formation of the vortex flow completely dominated by the parallel straight rolls in the entire cavity for the slightly supercritical buoyancy is shown in Fig. 6 for $Ra = 2000$. Note that it takes 600 s for the Rayleigh number to be raised from 0 to 2000. The results in Fig. 6 again suggest that at the beginning of the transient ($t = 0$) $Ra = 0$ and no flow motion is noted in the cavity (Fig. 6(a)). Shortly later, rectangular rolls along the cavity sides are successively induced (Figs. 6(b)–(e)). It is important to notice that at increasing time the shorter rolls near the short sides of the cavity gradually strengthen and extend towards the long sides of the cavity (Figs. 6(f) and (g)). And the rectangular rolls in the cavity core deform slowly and later become circular rolls (Fig. 6(h)). As the processes continue, the circular rolls degenerate slowly to become nearly straight rolls parallel to the short sides of the cavity (Figs. 6(i)–(k)). At this stage some irregularity in the roll pattern exists in the cavity core. Then, the slightly distorted rolls gradually straighten up and finally at $t > 4300$ s, a steady vortex flow in the form of entirely parallel straight rolls appears (Fig. 6(l)).

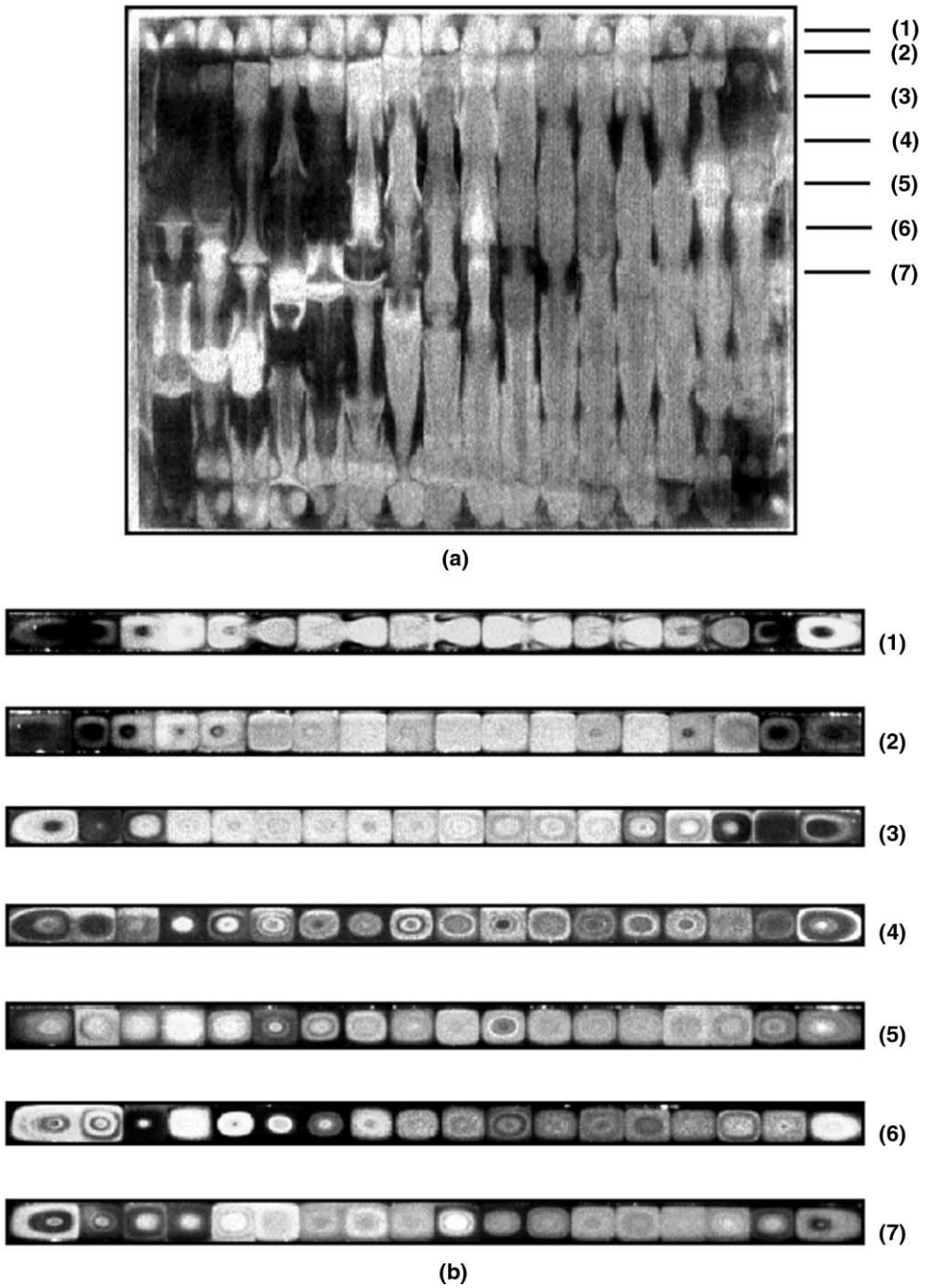

Fig. 3. Top and side view flow photos showing the parallel vortex rolls for $Ra = 2500$ respectively at $y = 0.5$ and $x =$ (1) 7.33, (2) 6.67, (3) 5.33, (4) 4, (5) 2.67, (6) 1.33 and (7) 0.

It is important to elucidate the wavenumber reduction processes at increasing buoyancy for the parallel roll pattern. This is illustrated by contrasting the flow formation at the higher Ra of 3000 shown in Fig. 7 with that in Fig. 6 for $Ra = 2000$. The results in Fig. 7 indicate that in the early stage of the vortex flow formation rectangular rolls again appear near the cavity sides (Fig. 7(b)). Slightly later, the rectangular rolls become stronger and more rectangular rolls are induced (Fig. 7(c)). Besides, weak parallel straight rolls

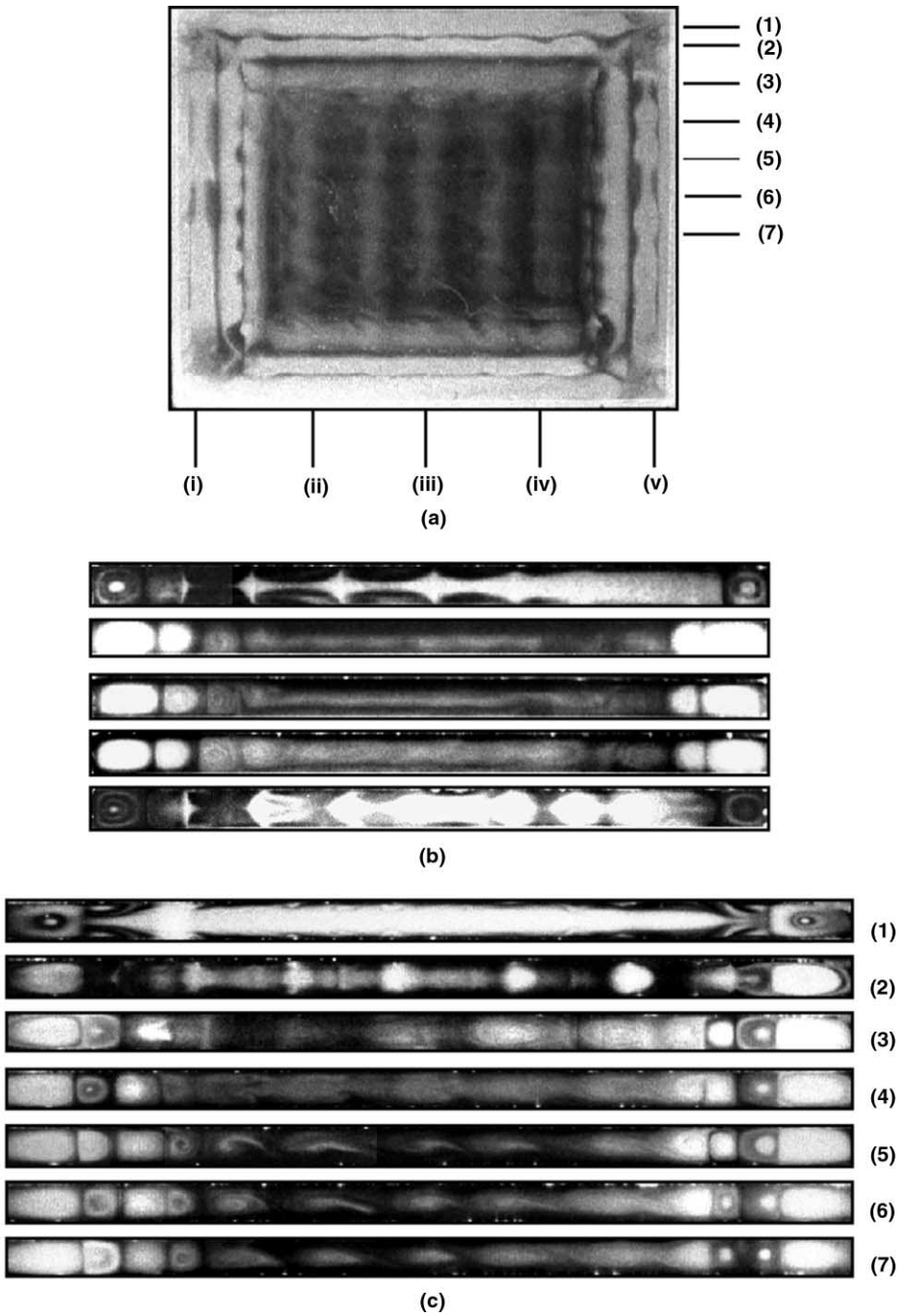

Fig. 4. Steady vortex flow for $Ra = 1500$ viewing from (a) the top at $y = 0.5$, (b) the short side at $z =$ (i) 1, (ii) 5.61, (iii) 10.09, (iv) 14.59 and (v) 19.07, and (c) from the long side at $x =$ (1) 7.33, (2) 6.67, (3) 5.33, (4) 4, (5) 2.67, (6) 1.33 and (7) 0.

are seen in the cavity core. At this stage the diameters of the rectangular and straight rolls are still equal to the cavity height. Note that under the continuing action of the buoyancy at increasing time the rectangular rolls away from the cavity sides become unstable and later split into cells (Figs. 7(d) and (e)). For a further increase in time the cells merge together into rolls which are larger than those induced in the previous stage (Fig. 7(f)). Meanwhile, the short legs of the rectangular rolls near the cavity sides grow in size

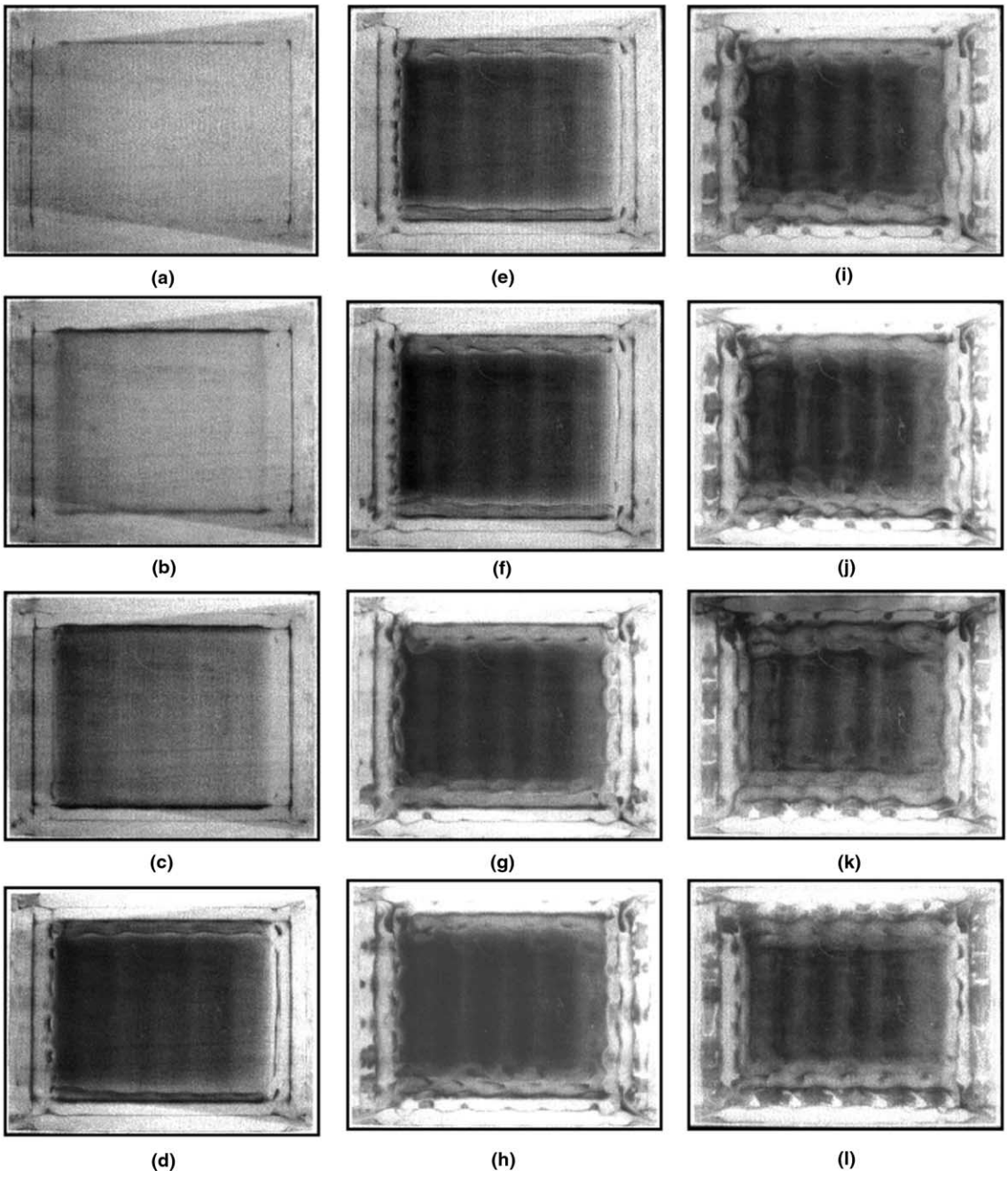

Fig. 5. Top view flow photos showing the formation of vortex flow following the raise of *Ra* from 0 to 1600 in 300 s for $t =$ (a) 23 s, (b) 136 s, (c) 325 s, (d) 558 s, (e) 677 s, (f) 856 s, (g) 1321 s, (h) 1832 s, (i) 2050 s, (j) 2459 s, (k) 2940 s and (l) 4653 s.

and extend gradually toward the long sides of the cavity. As this process continues, the long legs of the rectangular rolls weaken and shrink in size (Fig. 7(g)). Then the rolls become somewhat curved and are irregular to a certain degree (Figs. 7(h) and (i)). Later the curved rolls gradually adjust their orientations to align with the short sides of the cavity (Figs. 7(j) and (k)). Finally, a steady vortex flow consisting of parallel straight rolls in the entire cavity is formed (Fig. 7(l)). The above observation suggests that the roll expansion (wavenumber reduction) at increasing buoyancy is mainly related to the disintegration of the rolls into

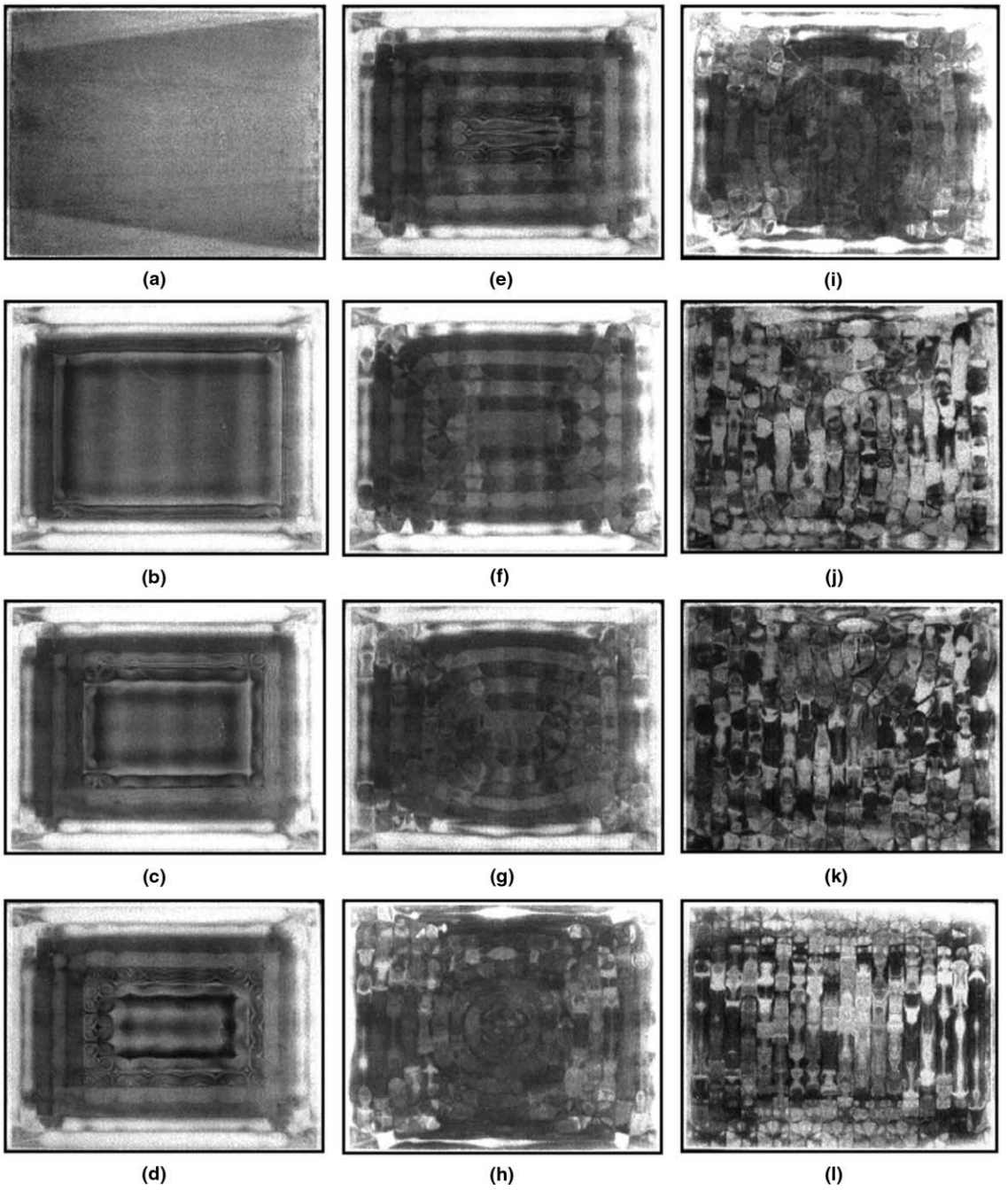

Fig. 6. Top view flow photos showing the formation of vortex flow following the raise of *Ra* from 0 to 2000 in 600 s for $t =$ (a) 0 s, (b) 123 s, (c) 424 s, (d) 506 s, (e) 656 s, (f) 849 s, (g) 935 s, (h) 1760 s, (i) 2063 s, (j) 3267 s, (k) 4020 s and (l) 4354 s.

cells at first and the subsequent merging of the cells into bigger rolls in the intermediate stage of the flow formation. This instability mechanism is different from that proposed by Leith et al. [31–33]. They reported that the skewed varicose instability began with the defects near the cavity sides followed with gliding or climbing motion of the defects in the flow.

Then, it is of interest to unveil how the serpentine roll is formed in the cavity core at certain *Ra* near the critical level. This is illustrated in Fig. 8 by showing the evolu-

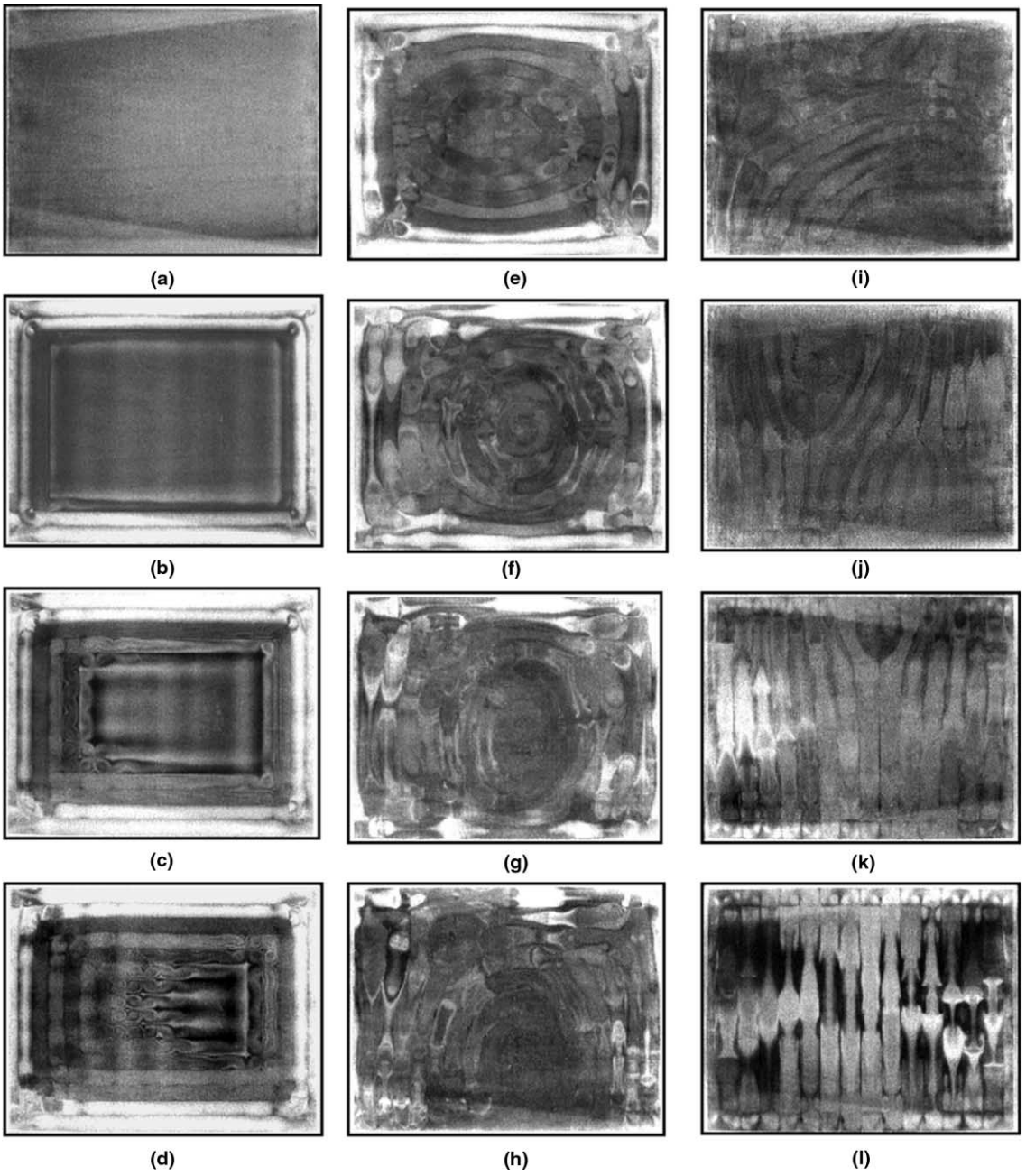

Fig. 7. Top view flow patterns showing the formation of vortex flow following the raise of *Ra* from 0 to 3000 in 800 s for $t =$ (a) 20 s, (b) 527 s, (c) 624 s, (d) 674 s, (e) 827 s, (f) 891 s, (g) 1114 s, (h) 1304 s, (i) 1939 s, (j) 3298 s, (k) 3608 s and (l) 4374 s.

tion of the vortex flow pattern when *Ra* is raised from 1500 to 1750. The results indicate that initially at $t = 0$, steady rectangular rolls surrounding the short parallel rolls already prevail in the cavity (Fig. 8(a)). Shortly after the Rayleigh number is raised, new rectangular rolls are induced adjacent to the existing ones (Figs. 8(b) and (c)). These newly induced rectangular rolls significantly squeeze the parallel rolls in the cavity core and cause them to become highly distorted. In fact, we have severely curved rolls in the cavity core at this stage (Fig. 8(d)). Later, the portions of the curved rolls parallel to the long sides of the cavity merge gradually with their neighboring rolls and a serpentine roll is finally formed in the cavity core (Figs. 8(e) and (f)).

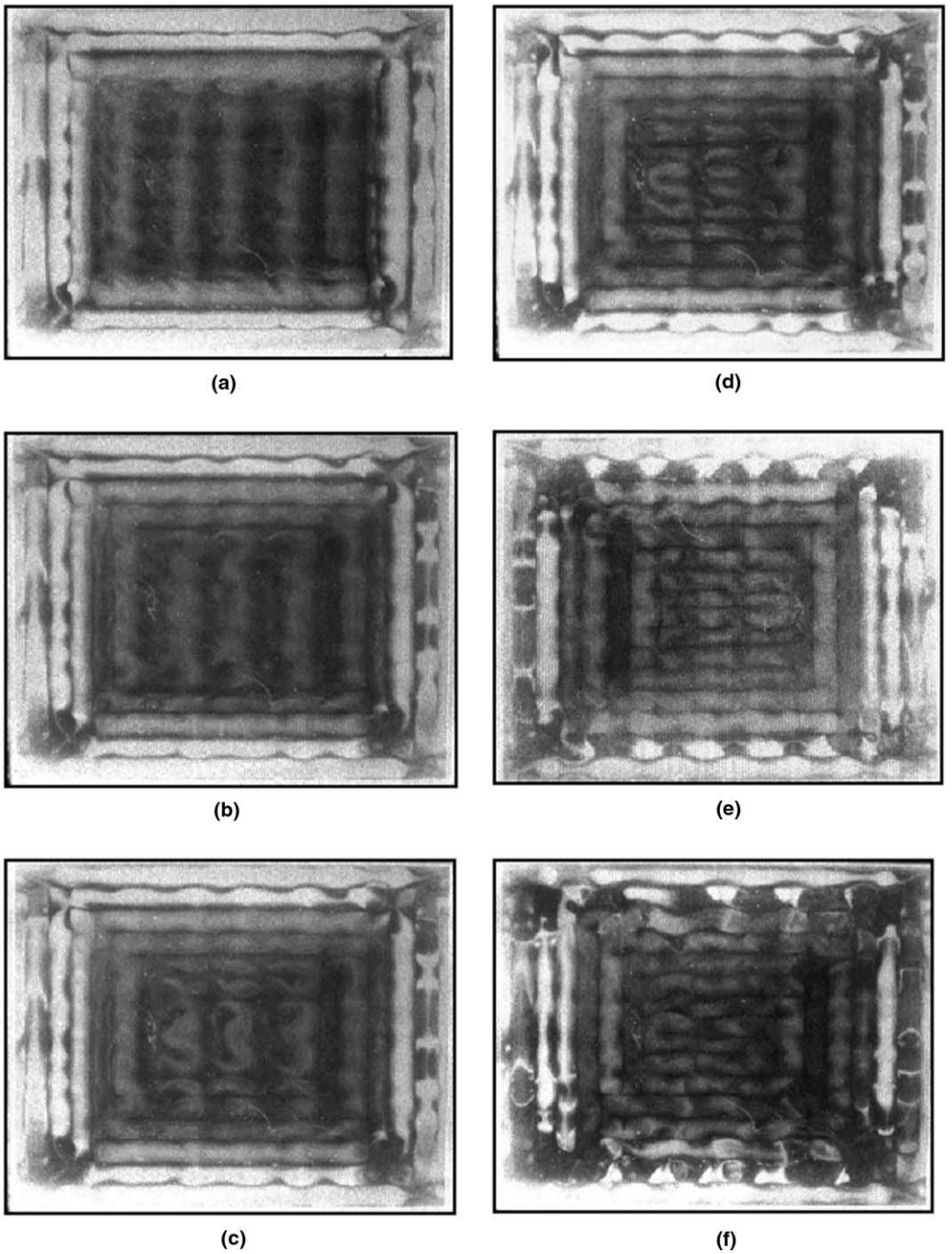

Fig. 8. Top view flow photos showing the formation of the serpentine roll in the cavity core by raising *Ra* from 1500 to 1750 in 300 s for t = (a) 0 s, (b) 235 s, (c) 559 s, (d) 746 s, (e) 1046 s and (f) 2823 s.

Finally, we examine how the heating rate in raising the Rayleigh number affects the evolution of the vortex flow patterns. This is demonstrated by comparing the flow formation photos in Figs. 6 and 9 induced at two very different heating rates for the parallel straight roll pattern for $Ra = 2000$. The results in Fig. 9 show that at the fast heating rate a few straight vortex rolls quickly form near the short sides of the cavity (Figs. 9(b) and (c)) while curved rolls appear in the cavity core. Later, rolls parallel to the long sides of the cavity gradually

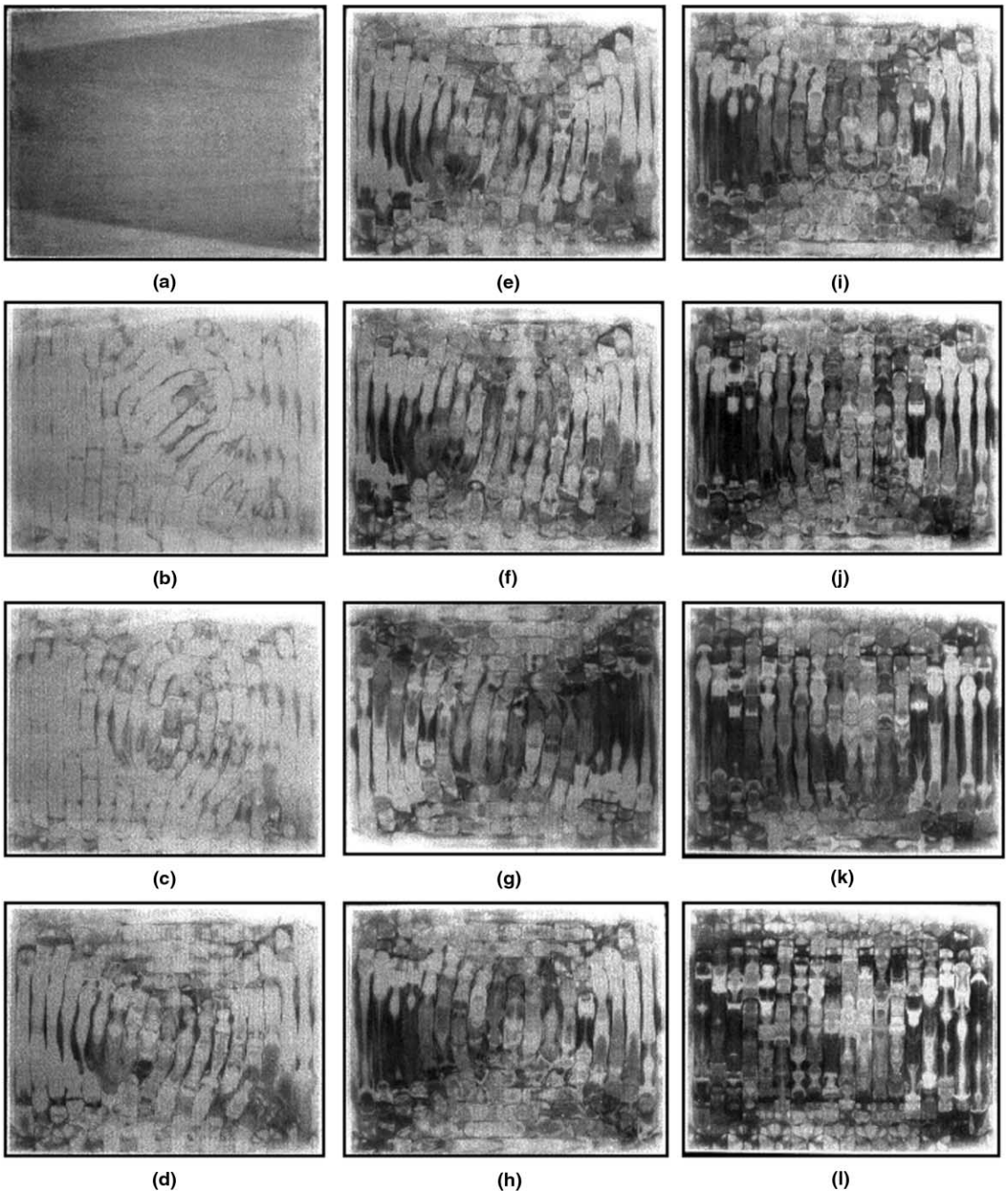

Fig. 9. Top view flow photos showing the formation of parallel rolls following the raise of *Ra* from 0 to 2000 in 30 s for $t =$ (a) 0 s, (b) 85 s, (c) 288 s, (d) 1023 s, (e) 1311 s, (f) 1555 s, (g) 2050 s, (h) 2328 s, (i) 2465 s, (j) 2667 s, (k) 3377 s and (l) 3779 s.

show up (Figs. 9(d)–(i)). As time proceeds, all the vortex rolls become stronger. Meanwhile, the rolls parallel to the short sides extend significantly towards the long sides of the cavity and the rolls parallel to the long sides of the cavity are slowly wiped out (Figs. 9(j) and (k)). Eventually, at $t > 3600$ s a parallel roll pattern consisting of 20 straight rolls forms. The above flow observation clearly indicates that the heating rate can substantially affect the vortex flow pattern during the intermediate stage of the flow formation processes. But the final vortex flow pattern remains the same for the change in the heating rate. Similar conclusion is reached

for the other vortex flow patterns observed in the present study.

4. Concluding remarks

Flow visualization has been carried out in the present study to explore the buoyancy-driven vortex flow patterns in a horizontal shallow cavity of air subject to bottom heating, covering both the slightly subcritical and supercritical states. The results clearly reveal the presence of the distinct vortex roll patterns even at subcritical buoyancy. In summary, for slightly subcritical Rayleigh number the vortex flow is in the form of rectangular rolls along the cavity sides encircling a number of short straight rolls all parallel to the short sides of the cavity. Near the critical Rayleigh number a serpentine roll prevails in the cavity core while at slightly supercritical state the entire cavity is filled with a number of straight rolls parallel to the short sides of the cavity. At even higher buoyancy the cavity is dominated by the irregular and time-dependent rolls. In addition, the complicate processes during the formation of various convection roll patterns were disclosed. The heating rate in raising the buoyancy force can significantly affect the vortex flow patterns during the intermediate stage of the flow formation processes. Moreover, the wavenumber reduction at increasing buoyancy for the parallel roll patterns was found to result from the splitting of some rectangular rolls into cells in certain period of time during the flow formation and later merging of the cells into bigger rolls.

Acknowledgements

The financial support for this study by the engineering division of National Science Council of Taiwan, ROC through the contract NSC83-0404-E009-054 is greatly appreciated.

References

[1] S. Ostrach, Natural convection in enclosures, ASME J. Heat Transfer 110 (4) (1988) 1175–1190.
[2] K.T. Yang, Transitions and bifurcations in laminar buoyant flows in confined enclosures, ASME J. Heat Transfer 110 (4) (1988) 1191–1204.
[3] E.L. Koschmieder, Bernard Cells and Taylor Vortices, Cambridge University Press, Cambridge, 1993 (Chapters 2–8).
[4] S.H. Davis, Convection in a box: linear theory, J. Fluid Mech. 30 (1967) 465–478.
[5] I. Catton, Convection in a closed rectangular region: the onset of motion, ASME J. Heat Transfer 92 (1) (1970) 186–188.
[6] R.P. Behringer, G. Ahlers, Heat transport and temporal evolution of fluid flow near the Rayleigh–Bénard instability in cylindrical containers, J. Fluid Mech. 125 (1982) 219–258.
[7] E.L. Koschmieder, S.G. Pallas, Heat transfer through a shallow horizontal convecting fluid layer, Int. J. Heat Mass Transfer 17 (1974) 991–1002.
[8] P. LeGal, A. Pocheau, V. Croquette, Square versus roll pattern at convective threshold, Phys. Rev. Lett. 54 (23) (1985) 2501–2504.
[9] D.B. White, The planform and onset of convection with a temperature-dependent viscosity, J. Fluid Mech. 191 (1998) 247–286.
[10] B.F. Edward, Crossed rolls at onset of convection in a rigid box, J. Fluid Mech. 191 (1988) 583–597.
[11] K. Stork, U. Müller, Convection in boxes: experiments, J. Fluid Mech. 54 (1972) 599–611.
[12] H. Oertel Jr., K. Bühler, A special differential interferometer used for heat convection investigations, Int. J. Heat Mass Transfer 21 (1978) 1111–1115.
[13] P. Kolodner, R.W. Walden, A. Passner, C.M. Sorko, Rayleigh–Bénard convection in an intermediate-aspect-ratio rectangular container, J. Fluid Mech. 163 (1986) 195–226.
[14] K.R. Kirchartz, H. Oertel Jr., Three-dimensional cellular convection in rectangular boxes, J. Fluid Mech. 192 (1988) 249–286.
[15] M.S. Chana, P.G. Daniels, Onset of Rayleigh–Bénard convection in a rigid channel, J. Fluid Mech. 199 (1989) 257–279.
[16] P.G. Daniels, C.F. Ong, Nonlinear convection in a rigid channel uniformly heated from below, J. Fluid Mech. 215 (1990) 503–523.
[17] M. Dubois, P. Bergé, Convection velocity field in the Rayleigh–Bénard instability: experimental results, Phys. Rev. Lett. 32 (19) (1974) 1041–1044.
[18] P. Bergé, M. Dubois, Experimental study of the velocity field in Rayleigh–Bénard convection, J. Fluid Mech. 85 (1978) 641–653.
[19] H.Q. Yang, K.T. Yang, J.R. Lloyd, Three-dimensional bimodal flow transitions in tilted enclosure, Int. J. Heat Fluid Flow 9 (1) (1988) 90–97.
[20] F.H. Busse, J.A. Whitehead, Instabilities of convection rolls in a high Prandtl number fluid, J. Fluid Mech. 47 (1971) 305–320.
[21] F.H. Busse, J.A. Whitehead, Oscillatory and collective instabilities in large Prandtl number convection, J. Fluid Mech. 66 (1974) 67–79.
[22] J.A. Whitehead, The propagation of dislocations in Rayleigh–Bénard rolls and bimodal flow, J. Fluid Mech. 75 (4) (1976) 715–720.
[23] F.H. Busse, R.M. Clever, Instabilities of convection rolls in a fluid of moderate Prandtl number, J. Fluid Mech. 91 (1979) 319–335.
[24] V. Croquette, H. Williams, Nonlinear waves of the oscillatory instability on finite convective rolls, Physica D 37 (1989) 300–314.
[25] J.N. Shadid, R.J. Goldstein, Visualization of longitudinal convection roll instabilities in an inclined enclosure heated from below, J. Fluid Mech. 215 (1990) 61–84.
[26] R.M. Clever, F.H. Busse, Low-Prandtl number convection in a layer heated from below, J. Fluid Mech. 102 (1981) 61–74.

[27] R.M. Clever, F.H. Busse, Nonlinear oscillatory convection, J. Fluid Mech. 176 (1987) 403–417.
[28] R.M. Clever, F.H. Busse, Three-dimensional knot convection in a layer heated from below, J. Fluid Mech. 198 (1989) 345–363.
[29] R. Farhadieh, R.S. Tankin, Interferometric study of two-dimensional Bénard convection cells, J. Fluid Mech. 66 (1974) 739–752.
[30] F.H. Busse, R.M. Clever, Instabilities of convection rolls in a fluid of moderate Prandtl number, J. Fluid Mech. 91 (1979) 319–335.
[31] J.R. Leith, Flow structure transition mechanisms in thermal convection of air in rectangular containers, Physica D 37 (1989) 334–340.
[32] J.R. Leith, Wavenumber evolution in Rayleigh–Bénard convection with air in moderate size containers, Int. Commun. Heat Mass Transfer 21 (2) (1994) 237–248.
[33] J.G. Maveety, J.R. Leith, Heat transfer in Rayleigh–Bénard convection with air in moderate size containers, Int. J. Heat Mass Transfer 41 (4&5) (1998) 785–796.
[34] S.J. Kline, F.A. McClintock, Describing uncertainties in single-sample experiments, Mech. Engrg. 75 (1953) 3–12.
[35] T.F. Lin, C.J. Liau, C.H. Yu, H.L. Su, Evolution of roll patterns in Rayleigh–Bénard convection in a rectangular layer: a numerical study, Numer. Heat Transfer A 29 (1996) 165–179.